Malaysian Journal of Chemistry, 2021, Vol. 23(2), 173-182
(Special Issue: *IKM Pahang Branch Online Symposium 2021 – Chemistry for Sustainable World*)

Structural Characterization and Visible Light-Induced Photoelectrochemical Performance of Fe-Sensitized TiO_2 Nanotube Arrays Prepared via Electrodeposition

Lim Ying Chin[1*], Najaa Mustaffa[1], Asmaa Kadim Ayal[2], Devagi Kanakaraju[3] and Lim Ying Pei[4]
[1]Faculty of Applied Sciences, Universiti Teknologi MARA, 40450 Shah Alam, Selangor, Malaysia
[2]Department of Chemistry, College of Science for Women, University of Baghdad, Al-Jadriya Campus, Baghdad, Iraq
[3]Faculty Resource Science and Technology, Universiti Malaysia Sarawak, 94300 Kota Samarahan, Sarawak, Malaysia
[4]Faculty of Chemical Engineering, Universiti Teknologi MARA, 40450 Shah Alam, Selangor, Malaysia
*Corresponding author (e-mail: limyi613@uitm.edu.my)

Surface modification of TiO_2 nanotube arrays via metal doping is one of the approaches to narrow the wide bandgap of TiO_2 in order to increase its adsorption to the visible region. The present work focuses on the fabrication of a Fe-sensitized TiO_2 nanotube arrays (Fe-TNT) photoanode. Ordered Fe-TNTs were successfully synthesized using a facile two-step electrochemical method by varying the deposition voltage (2-4 V). The morphology, structure, composition, and visible light response were characterized by field-emission scanning electron microscopy (FESEM), X-ray diffraction (XRD), energy-dispersive X-ray spectroscopy (EDX), UV-Vis diffusion reflection spectroscopy (DRS), and photoelectrochemical (PEC) test. The XRD investigation demonstrated that the sensitization of Fe did not destroy the nanotube array structure, and the Fe-TNTs had an anatase phase composed of cubic-like particles at higher deposition voltages. The UV–Vis absorption spectra of the Fe-TNTs showed a redshift of photoresponse towards visible light. Such a redshift was characterized by a decrease in bandgap energy and the photo efficiency was enhanced. The optimal photoelectrochemical performance was observed at 2.5 V deposition voltage for 10 minutes and surpassed that of pristine titania nanotube arrays. The present work demonstrates feasible modification of TiO_2 with Fe as a potential photoanode in solar conversion devices.

Key words: Electrodeposition; titania nanotubes; photoelectrochemical; iron

Received: November 2020; Accepted: January 2021

Water photolysis using titanium dioxide (TiO_2) was first discovered five decades ago by Honda and Fujishima, and thereafter TiO_2 has attracted worldwide attention as the research demonstrated the possibility of producing hydrogen as a renewable source of energy from water upon light illumination [1]. TiO_2 possesses high photochemical stability, long-term thermal stability, non-toxicity, and high photocatalytic activity in the ultraviolet region. It is an important and efficient semiconductor with widespread applications in various fields such as sensing, solar conversion devices, photocatalyst for environmental remediation, biomaterials, and antibacterial coating [2,3]. Nanostructured TiO_2 can be found in various forms, for instance in nano powder and thin films. However, nanostructured TiO_2 thin films are more desirable for industrial applications compared to TiO_2 nano powder, as the latter tends to agglomerate easily due to high surface energy [4]. Nanostructured TiO_2 thin films in the form of nanowires, nanobelts, and nanotubes are desired for wide applications due to its distinctive geometry, large surface-to-volume ratio, remarkable charge transfer, high sensitivity, and also high surface activity. Particularly, TiO_2 nanotube (TNT) is known to be one of the most promising nanostructured oxides where the tubular structure is anticipated to minimize electron-hole recombination by facilitating the movement of electrons in a unidirectional way [5]. Over the past decades, the synthesis of highly ordered TiO_2 nanotube array films has attracted fascinating attention to be used as photocatalysts in the area of energy and environment [4,6,7]. Nonetheless, there are two significant pitfalls associated with the extensive use of TiO_2 for industrial applications. First, the relatively large TiO_2 bandgaps of 3.2 eV for the anatase phase and 3.0 eV for the rutile phase [7] have limited its efficient photocatalytic reactions in the visible region. Thus, UV light is needed to activate TiO_2 for any

†Paper presented at the IKM Pahang Branch Online Symposium 2021 – Chemistry for Sustainable World

photo-related reactions, which accounts for only a small fraction of the solar light. Second, low electron mobility (0.3 $cm^2V^{-1}s^{-1}$) and rapid recombination of electron-hole in TiO_2 remarkably decrease its quantum efficiency [8]. In order to minimize the electron-hole recombination, as well as extending the practical application of TiO_2 for efficient use of solar energy, it is indispensable to enhance the photoresponse of TiO_2 to the visible light region by tuning the electronic structure of TiO_2.

One way to extend the spectral response of TNT is by modification with narrower bandgap materials including CdS, WO_3, CdSe, and PbS [9-12]. In addition, non-metal doping using carbon, phosphorus, sulfur, and nitrogen [13], and transition metal doping including copper (Cu), manganese (Mn), nickel (Ni), iron (Fe), and vanadium (V) have been used to increase the photoelectrochemical efficiency of TNTs [14-16]. Generally, the modification of TiO_2 with transition metals is believed to modify the energy level through the generation of a new forbidden gap. Among these elements, Fe is considered as a potential dopant because it is readily available and inexpensive. Furthermore, the ionic radii of Fe^{3+} (0.64 Å) and Ti^{4+} (0.68 Å) are similar, and thus Fe^{3+} can be conveniently incorporated into the crystal structure of TiO_2 without damaging its lattice [17]. It was experimentally observed that Fe exhibits phase transformation under certain conditions, and with a small amount Fe can act as a temporary photo-generated electron or hole-trapping site which inhibits the charge recombination [18], in addition to narrowing the bandgap of TNT. For example, Bashiri *et al.* (2020) indicated that Fe_2O_3-modified TNT produced higher photocurrent density, low charge transfer resistance, and a long lifetime of the photoexcited electron [19]. Similarly, Tong *et al.* (2020) reported that the loading of Fe on TNT films shifted the optical absorption edge towards the visible region and narrowed the bandgap energy of TNTs from 3.10 eV to 2.85 eV [20].

Till now, literature search found that various methods have been reported on the fabrication of Fe-TNTs including hydrothermal, solvothermal, impregnation-calcination, sol-gel, and electro-deposition [21-23]. Among all these methods, electrodeposition method is favorable as it is highly practical, consumes less energy, and requires relatively shorter time for synthesis. To date, very few reported works have been published on the use of electrodeposition technique and the effects of preparation conditions on the photoelectrochemical properties of Fe-TNTs. For example, there is only one research work on the anodic and cathodic deposition of amorphous Ti oxyhydroxide gel (TiOx) and iron oxyhydroxide (FeOOH), reported by Vasile *et al*. (2020) [24]. In this work, we propose a facile electrodeposition method to fabricate Fe-sensitized TNTs by using anodized TNTs as the substrate and $FeCl_3$ as the iron precursor. The relationship between the electrodeposition voltage and the physicochemical properties was investigated and compared. Additionally, the photoelectrochemical performance of the samples was also evaluated under visible light illumination to verify their application as photoanodes.

MATERIALS AND METHODS

1. Preparation of Fe-TNTs

Fe-TNTs were prepared using a facile two-step electrochemical method. TNTs were first prepared using anodization previously reported by our group [25]. Briefly, rectangular samples of titanium foils (10 mm × 20 mm, 99.5% purity, Sigma Aldrich) were cleaned by ultrasonication in acetone, isopropanol, and deionized water for 15 minutes, respectively. The volume used for each solvent during ultrasonication was fixed at 15 mL. Then, anodization of titanium was carried out in a standard two-electrode cell using Ti foil as the anode and high-density graphite as the cathode. Anodization was performed in a mixture of electrolytes, which was prepared by mixing a 1:1 ratio of ethylene glycol and glycerol and 0.5 wt.% NH_4F at 20 V for 30 minutes. The selection of this electrolyte mixture aimed to decrease the current fluctuation during the anodization. After anodization, the as-formed samples were rinsed with deionized water and subsequently dried in air followed by calcination in air at 500°C for 2 hours. The calcination process is crucial to induce crystallinity in titania nanotubes (TNTs) and the selection of 500°C aimed to produce TNTs with crystalline anatase while maintaining the tubular structure of TNTs. Subsequently, the earlier prepared TNTs were used as the substrate for the sensitization of TNTs with iron using the electrodeposition method. In a typical synthesis, electrodeposition of iron was carried out in a typical two-electrode cell where graphite was placed at the anode while the calcined TNTs were placed at the cathode in an electrolytic medium containing 0.1 M $FeCl_3$ solution (used as the iron source). To determine the effect of the deposition voltage on the formation and morphology of Fe-TNTs, electrodeposition of iron was carried out at various voltages, namely 2 V, 2.5 V, 3 V, and 4 V for 10 minutes, and Table 1 summarizes the experimental conditions for 4 different Fe-TNT samples.

Table 1. Deposition parameters for the synthesis of different Fe-TNTs

Samples	Electrodeposition condition
TNT (control)	-
Fe-TNT1	2 V, 0.1 M $FeCl_3$, 10 mins
Fe-TNT2	2.5 V, 0.1 M $FeCl_3$, 10 mins
Fe-TNT3	3 V, 0.1 M $FeCl_3$, 10 mins
Fe-TNT4	4 V, 0.1 M $FeCl_3$, 10 mins

2. Characterization of TNTs and Fe-TNTs

The phase composition identification of the TNT and Fe-TNT samples was performed using the X-ray diffraction (XRD, PANalytical X'pert Pro) with a Cu Kα radiation (λ = 0.154 nm). The XRD pattern data were collected from the scanning 2θ range between 10° and 80°, with a rate of 0.04° per second. Field emission scanning electron microscopy (FESEM) analysis was performed using Carl Zeiss SUPRA 40VP to analyze the surface morphology of the samples. A low electron beam voltage of 5 kV was used, and thus no coating was required before the imaging. Quantitative analysis of elements was carried out with Energy Dispersive X-ray (Oxford INCA Energy 200 EDX) attached with FESEM. In addition, the samples were also analyzed using Shimadzu UV-3600 spectrophotometer operated in the wavelength range from 200 to 800 nm with $BaSO_4$ as a reflectance standard to determine the changes in the bandgap of TNTs after sensitization with Fe. The bandgap energy could be obtained by extrapolating the straight-line portion of the sharp absorption edge in a plot of absorbance (A) against wavelength (nm) using the following equation:

$$E_g = 1240/\lambda \quad (1)$$

Where, E_g is the bandgap width (eV) and λ is the absorption band wavelength.

3. Photoelectrochemical Measurement

The photoelectrochemical performance of Fe-TNTs was measured using a conventional rectangle three-electrode cell consisting of the prepared Fe-TNTs as the photoanode (working electrode), a platinum wire counter electrode, and an Ag/AgCl reference electrode. The working electrode was illuminated with a 300 W halogen lamp placed 15 cm away from the cell. The photocurrent was measured with scanning potentiostat (Autolab PGSTAT 101) with a voltage sweep from +1.0 V to −1.0 V at a sweep rate of 50 mV/s. The photoconversion efficiency of all samples was calculated by using the formula:

$$\text{Photoconversion efficiency } (\eta\%) = I_o\,(1.23\text{-}V_{bias})/J_{light} \times 100\% \quad (2)$$

Where, I_o = current density (mA/cm^2); V_{bias}= applied potential; J_{light} = 150 mW/cm^2; and 1.23 V is the standard electrode potential for water splitting.

RESULTS AND DISCUSSION

1. The Appearance of TNTs and Fe-TNTs

The fabrication of TNTs by anodization was done in a mixture of glycerol and ethylene glycol at 20 V. The TNTs were then used as the substrate for the deposition of Fe with $FeCl_3$ as the source of Fe. From Figure 1(a), the Ti foil showed a lustrous silvery-grey appearance and there was a visible color change of films after the anodization and electrodeposition process. At first, the shining silver of Ti film changed to dark yellow upon anodization. Then, the color of the film changed from dark yellow to dark blue after calcination at 500°C in the furnace, indicating that crystallinity of TiO_2 was successfully induced upon calcination. The TNT samples obtained from both the anodization and calcination appeared to be visually homogeneous. No obvious change in the color of undoped TNT to Fe-TNT. Upon deposition of Fe, Fe-TNT appeared darker with more uniform dark blue as compared to calcined TNT, suggesting that the electrodeposition of Fe was successful. The layer thickness of Fe-TNT appeared to be good as well, as shown in Figure 1(b). Furthermore, when deposition voltage was varied at 2 V, 2.5 V, 3 V, and 4 V at 10 minutes deposition time, the films became darker and severed when a higher voltage was applied. There was no obvious change in the appearance for Fe-TNT1, Fe-TNT2, and Fe-TNT3. At a higher voltage of 4 V, the site on the film surface became black and was not evenly formed. It also showed the sign of corrosion as depicted along the right side of the surface, which might be ascribed to a vigorous reaction at 4 V. It is postulated that iron probably not well doped and deposited without proper orientation on the surface of TNT upon electrodeposition. These strong deposition and crystal growth reaction are anticipated to affect the photoelectrochemical properties and also the stability of the nanotube as a photoactive electrode.

2. FESEM Analysis

The effect of sensitization of Fe with TNT was analyzed by FESEM to examine its effect on the surface morphology of TNT. Figure 2 shows the FESEM images of calcined TNT and Fe-TNTs prepared at different deposition voltages.

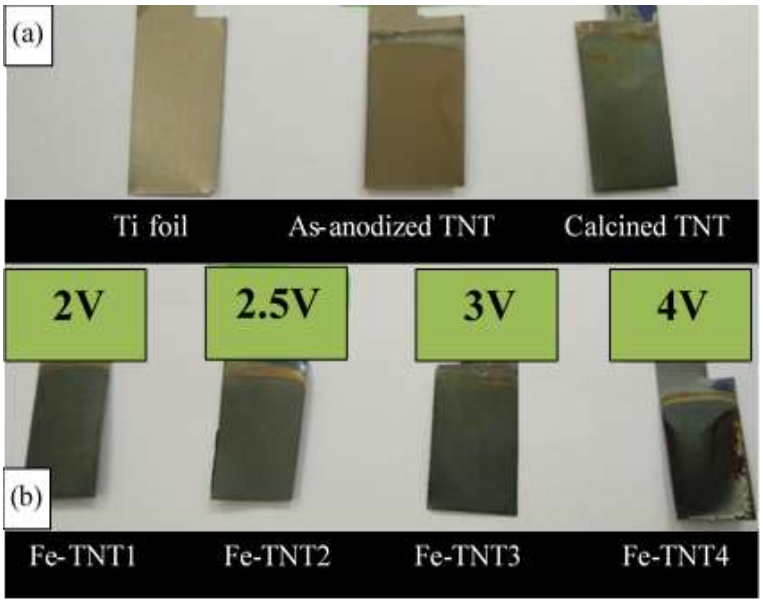

Figure 1. Color changes of films after: (a) anodization and calcined process; and (b) the appearance of Fe-TNTs after electrodeposition at various voltages

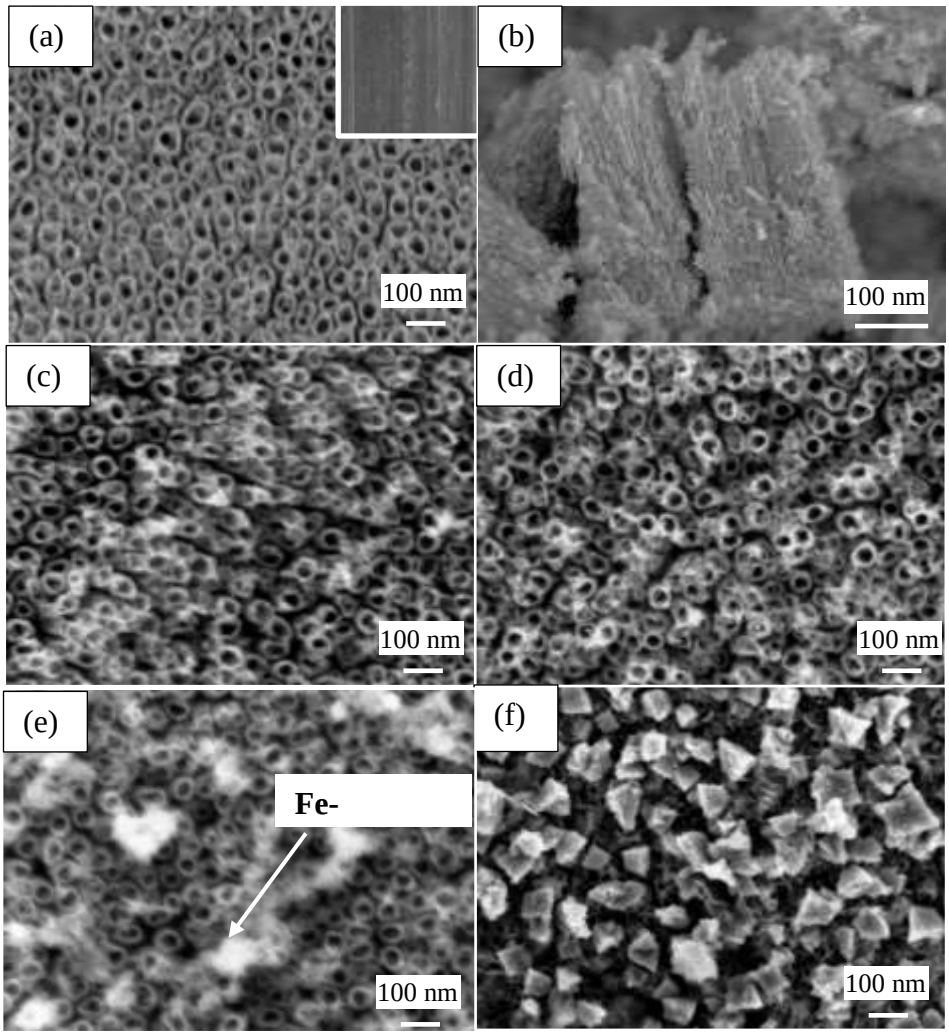

Figure 2. FESEM images at 50K magnification of: (a) calcined TNT (inset is Ti foil); (b) cross-section of TNT; and Fe-TNT films prepared at different deposition voltages: (c) 2 V, (d) 2.5 V, (e) 3 V, and (f) 4 V

The smooth surface was observed for blank Ti initially, as shown in the inset in Figure 2(a). Upon anodization at 20 V in a mixture of ethylene glycol, glycerol, and NH_4F solution, ordered TNT with wall thickness of 18 ± 5 nm was observed with outer and inner diameters of 93 ± 11 nm and 54 ± 9 nm, respectively. Well-aligned and vertically oriented nanotubes were formed as proven by the cross-sectional FESEM image in Figure 2(b). Thereafter, the TNT was used as the substrate for electrodeposition of iron at different deposition voltages for 10 minutes in 0.1 M $FeCl_3$ solution. As shown in Figures 2(c)-(e), all Fe-TNT samples seemed to be relatively less ordered compared with TNT, however no discernible changes in the nanotube morphology. The amount of Fe particles attached on both Fe-TNT1 and Fe-TNT2 samples appeared to be comparable and less visible. On increasing to 3 V, more obvious Fe particles were observed to be randomly scattered on the surface of nanotube upon electrodeposition, indicating successful deposition of Fe. Defined cubic-like Fe particles were observed for Fe-TNT4 and were clumped together on the top surface of the nanotube and almost obscured the underlying nanotubes, as evidenced from the black surface appearance of Fe-TNT4 (Figure 2(f)). The clumping and full coverage of Fe particles on the mouth of nanotubes are undesirable as this could hinder and prevent light from reaching the nanotubes and subsequently resulting in lower light adsorption by Fe-TNT4 sample. Consequently, it is anticipated that photo efficiency will be reduced as well.

3. XRD Analysis

The phase composition and crystallinity of the prepared TNTs and Fe-TNTs were evaluated by using X-ray diffractometry. Figure 3 shows the XRD patterns of the TNTs and the Fe-TNTs prepared at various deposition voltages. The formation of anatase TiO_2 at 25.4° and 48.4° (JCPDS No. 21-1272) was observed for all deposition voltages. Diffraction from the underlying metallic titanium (JCPDS No. 44-1294) was also visible. However, all Fe-TNT samples showed no diffraction peaks pertaining to any iron-containing species, suggesting that the Fe ions might have been incorporated in the TNT anatase structure or highly dispersed in the TiO_2 matrix [26]. This phenomenon is possible as the radius of Fe^{3+} (0.64 Å) is comparable to Ti^{4+} (0.68 Å). It is noteworthy to mention that the deposition of Fe on TNT has resulted in an increase in anatase signal for Fe-TNT3 when compared to TNT, indicating a higher crystallinity with iron deposition. From the literature, such an increase in intensity is an indicator of iron ions insertion in the oxide framework, which may in return accelerates the crystallization of anatase [26]. Our finding, however, contradicts the work reported by Wang *et al*. (2017), who demonstrated the intensity of anatase signal decreases upon Fe deposition [21]. This is probably ascribed to different synthesis methods employed where solvothermal approach using the same iron precursor ($FeCl_3$) was used by the author instead of electrodeposition in this study. However, for Fe-TNT4 sample that showed the presence of a greater amount of cubic-like Fe particles deposited, the anatase (101) peak intensity was weaken compared to TNT and the other Fe-TNT samples. Crystallite sizes were estimated by using the Debye Scherer equation:

$$D = k\lambda/\beta\cos\theta \qquad (3)$$

Where, k is the shape factor of 0.9, λ is the X-ray wavelength, β is the full width at half maximum of diffraction peak relating to the (101) anatase peak, and θ is the diffraction angle.

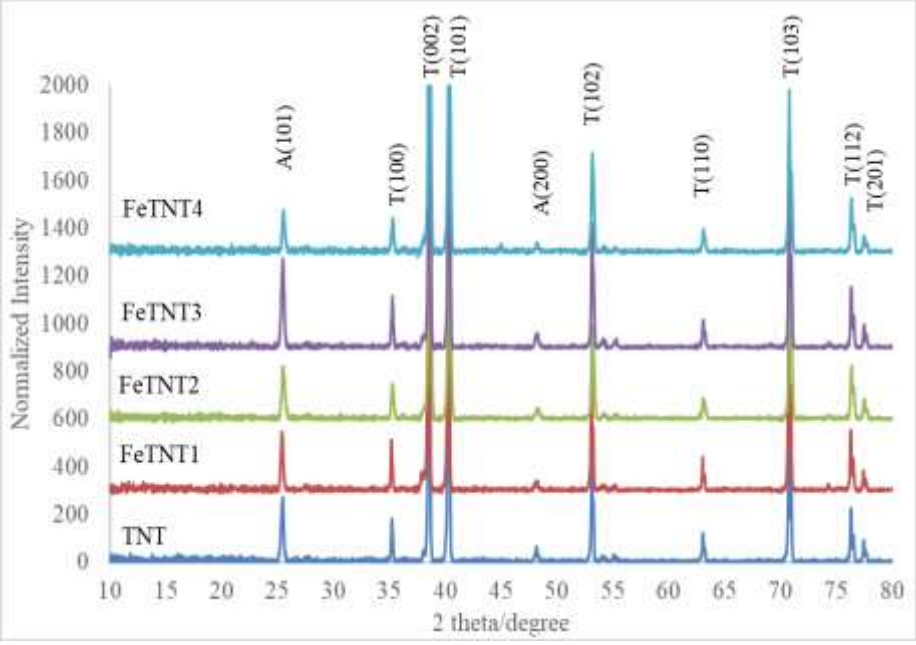

Figure 3. XRD patterns for TNT and Fe-TNT thin films

Table 2. Elemental compositions of TNT and Fe-TNT samples prepared at different deposition voltages obtained in EDX analysis

Sample	Atomic %		
	O	Ti	Fe
Pure TNT	39.46	60.54	Not detected
Fe-TNT1	42.63	56.08	1.29
Fe-TNT2	38.95	58.36	2.69
Fe-TNT3	43.19	53.49	3.32
Fe-TNT4	9.58	10.59	79.83

The estimated crystallite size for TNT was 32.5 ± 1.3 nm and decreased with deposition voltage to 30.2 ± 1.2, 29.0 ± 1.4, and 23.2± 1.3 nm for Fe-TNT1, Fe-TNT2, and Fe-TNT3, respectively. A decrease in crystallite size shows that iron ions appear to inhibit the growth of TNT crystallite, a similar effect has also been reported by Tong *et al*. (2020) [21]. This observation demonstrated that Fe particles have been successfully distributed on the TNT matrix.

4. Elemental Compositional Analysis

EDX analysis was performed to determine the elemental composition present in the TNT and Fe-TNT samples, as tabulated in Table 2. As expected, the amount of Fe deposited on TNT increased with increasing deposition voltage. This is due to the fact that higher voltage leads to a higher reaction rate and thus more Fe could be deposited on the surface of TNT. However, at the highest voltage of 4 V, the deposition rate was too intense, as well as the crystal growth was too rapid, and therefore large and distinct cubic-like particles could be seen, as shown in Figure 2(f). A very high amount of Fe particles is unfavorable as this might become the recombination centers for photogenerated charge carriers. Ti and O originated from TNT were also detected for all samples. For pure TNT, Fe-TNT1, Fe-TNT2 and Fe-TNT3, the Ti and O contents were almost similar. Meanwhile, for Fe-TNT4, the atomic % of Ti and O had reduced substantially, which was almost 5 times lower compared to its pure TNT counterpart, which was ascribed to a large amount of Fe particles deposited on the surface of TNT.

5. UV-Vis Diffuse Reflectance Analysis

The optical behaviors of TNT and Fe-TNT samples were analyzed by overlay UV-Vis diffuse reflectance spectra, as shown in Figure 4. TNT primarily showed high absorption in the ultraviolet region with an absorption edge below 390 nm, corresponding to the bandgap of 3.18 eV. Fe-TNT1 and Fe-TNT3 exhibited a redshift with obvious higher visible light absorption (500-800 nm) compared to TNT, corresponding to a reduced bandgap of 2.95 and 2.93, respectively. In the case of Fe-TNT2, the bandgap was anticipated to be between 2.90 to 3.00 on the basis of EDX, XRD and FESEM analyses. The estimated bandgap values were further supported by research findings from other researchers which obtained almost similar morphologies and crystal structures [20, 21, 27]. For instance, the work of Tong *et al*. (2020) demonstrated that Fe-TNT produced by anodization followed by $Fe(NO_3)_3$ immersion has a bandgap of around 2.8 eV to 3.0 eV. For Fe-TNT fabricated by simultaneous anodization and deposition, the Fe-TNT exhibited a bandgap of 2.90 to 3.05 with no reflection pertaining to iron species from the XRD analysis. The crystal structure and morphological analysis of this study are in good agreement with our finding [28]. This reduction of the bandgap indicated that Fe-TNT1 and Fe-TNT3 should demonstrate higher photo response under halogen lamp illumination. Nonetheless, Fe-TNT4 had the lowest visible light absorption among all the samples and the bandgap obtained was similar to that of TNT, as shown in Table 3. Efficient Fe deposition that resulted in a reduced bandgap suggested that a certain amount of defect states may be introduced, which in return can act as a trapper for charger carriers [29].

6. Photoelectrochemical Test of Fe-TNTs

The photoelectrochemical performance of Fe-TNTs was evaluated by using linear sweep voltammetry to verify the application of TNT and Fe-TNT as a photoactive electrode. Figure 5 shows the photocurrent density recorded in the potential range between −1 to 1V versus Ag/AgCl for Fe-TNTs prepared at different voltages. The light was intermittently cut at a constant frequency and the immediate surge and drop of the photocurrent were in accordance with the intervals of light-on and light-off. All samples exhibited a fast response and excellent charge and discharge transfer as proven by instant increased current density upon light illumination and decreased current density when the light was switched off.

In general, the photoelectrochemical performance of an electrode relies on the following factors: light absorption and electron/hole pairs mobility and their recombination rate. Apparently, all Fe-TNT samples demonstrated higher photocurrent in comparison with TNT except for Fe-TNT4. Fe-TNT2

showed the highest photocurrent and photoconversion efficiency (Table 3) among all the synthesized samples, suggesting that more photoinduced charges were generated and the recombination between the electrons and holes was prevented [28]. Fe^{3+} trapped the photogenerated electrons and holes that reduced the recombination rate of the photogenerated charge carriers. Meanwhile, for Fe-TNT4, the current density curve was odd and showed a distinct difference from the usually observed curve. The large amount of Fe deposited, as shown in the EDX analysis, is believed to hinder the charge transport and facilitate greater charge recombination.

When Fe^{3+} amount exceeds a certain level, Fe^{3+} may also act as the recombination center for the photogenerated electrons and holes due to the decrease of the distance between trapping sites [27]. When Fe-TNTs were irradiated with the light source, electron-hole pairs were generated and the reaction that took place is described in the following equations:

$$TiO_2 + hv \rightarrow e^-_{cb} + h^+_{vb} \quad (4)$$

$$Fe^{3+} + h^+_{vb} \rightarrow Fe^{4+} \quad (5)$$

$$Fe^{4+} + OH^- (ads) \rightarrow Fe^{3+} + OH\cdot(ads) \quad (6)$$

$$Fe^{3+} + e^-_{cb} \rightarrow Fe^{2+} \quad (7)$$

$$Fe^{2+} + O_2 (ads) \rightarrow Fe^{3+} + O_2^- \quad (8)$$

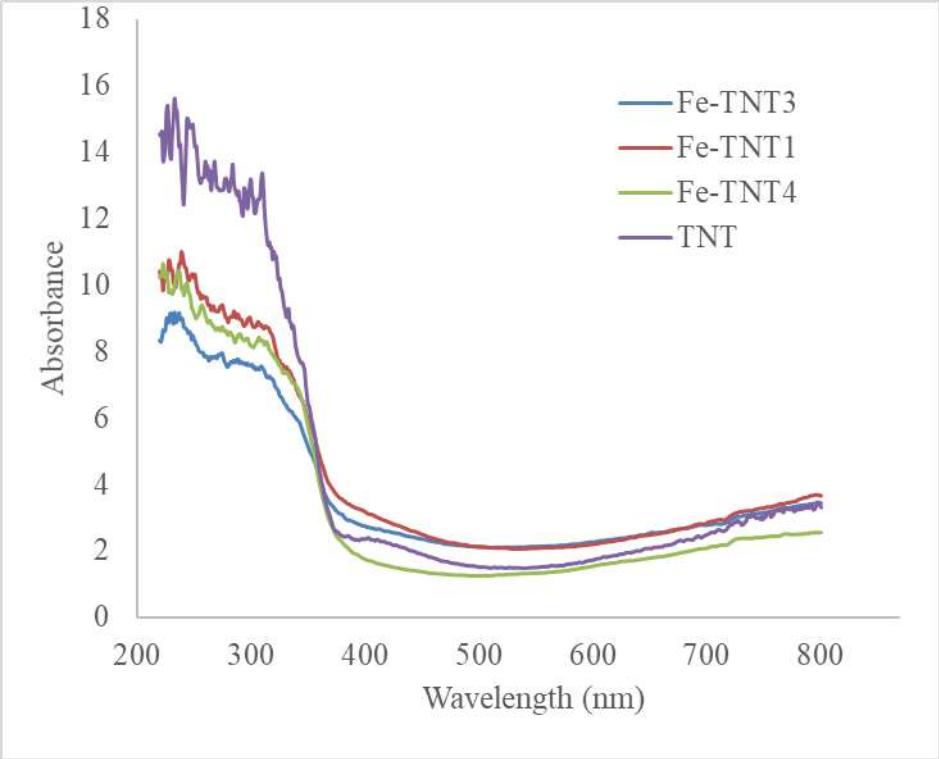

Figure 4. UV-Vis spectra for TNT and Fe-TNT samples

Table 3. Photocurrent density, photoconversion efficiency, and bandgap calculated for TNT and Fe-TNTs prepared at different deposition voltages

Sample	Photocurrent Density (mA/cm^2)	Photoconversion efficiency (η %)	Bandgap (eV)
TNT	2.4×10^{-2}	1.5×10^{-2}	3.18
Fe-TNT1	3.9×10^{-2}	2.4×10^{-2}	2.95
Fe-TNT2	6.5×10^{-2}	4.0×10^{-2}	-
Fe-TNT3	4.4×10^{-2}	2.8×10^{-2}	2.93
Fe-TNT4	9.5×10^{-3}	5.9×10^{-3}	3.10

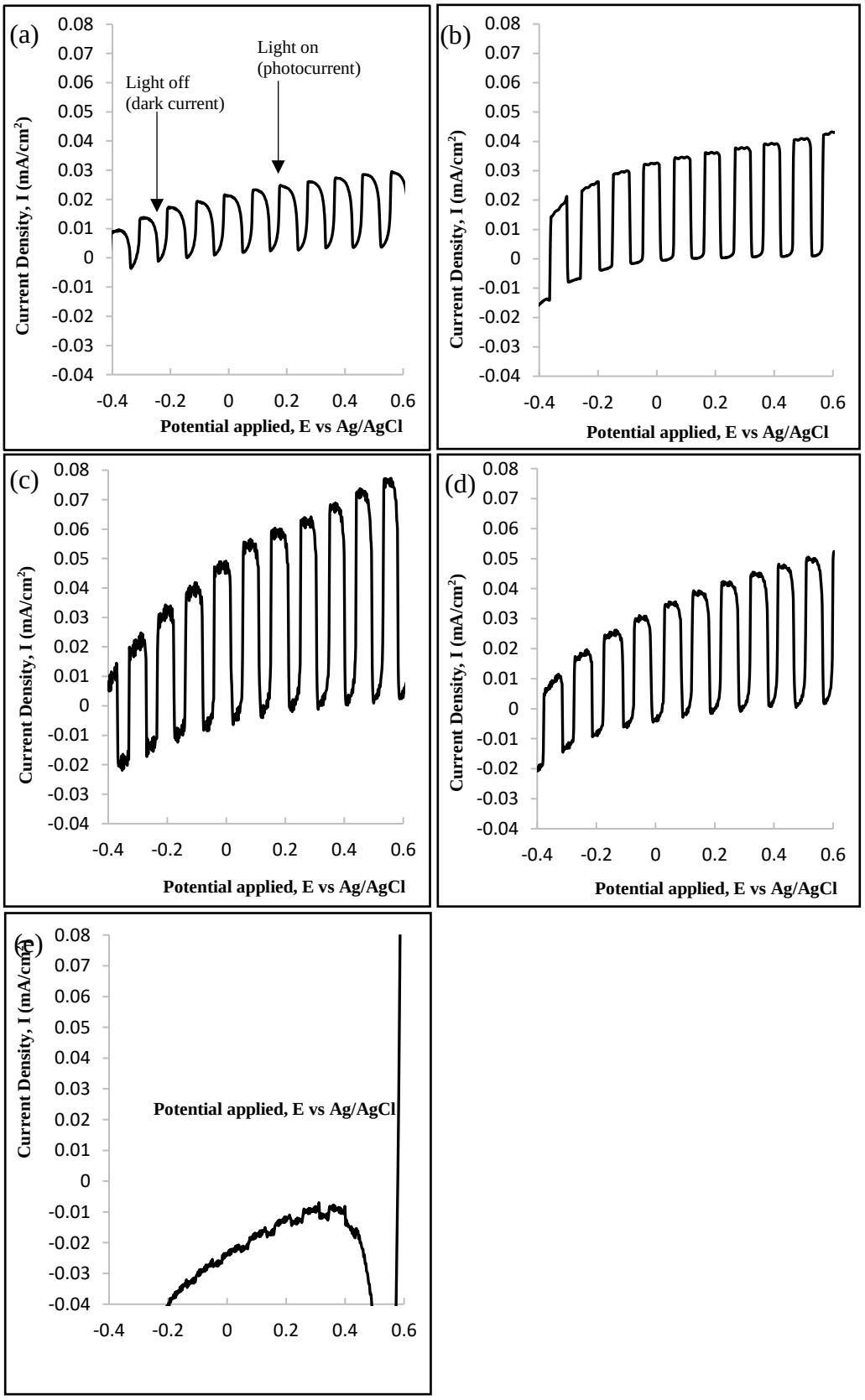

Figure 5. Current density curves of: (a) pure TNT; and Fe-TNTs prepared at different deposition voltages: (b) Fe-TNT1, (c) Fe-TNT2, (d) Fe-TNT3, and (e) Fe-TNT4

After electrons are excited from the valence band (vb) to the conduction band (cb) and leave holes, Fe^{3+} tends to trap the holes. These trapped holes in Fe^{4+} can produce hydroxyl radicals upon migrations to the TiO_2 surface and absorbing OH^-. At the same time, Fe^{3+} can also trap photogenerated electrons producing Fe^{2+}. Subsequently, Fe^{2+} could be oxidized to Fe^{3+} by transferring electrons to adsorbed O_2 on the surface of TiO_2. Among the three different chemical states of Fe ions (i.e., Fe^{2+}, Fe^{3+} and Fe^{4+}), Fe^{3+} is relatively more stable due to its $3d^5$ electronic configuration. As such, the charges trapped by Fe^{2+} and Fe^{4+} (which are relatively unstable) can easily return to Fe^{3+}, and thus inhibit the recombination of photogenerated electron-hole. However, when a very high amount of Fe is being deposited, Fe^{3+} can act as a center of recombination of photogenerated carriers [28], as can be seen from the simultaneous reaction that could happen from equations 5, 7, 8, and 9, which is unfavorable for any photoelectrochemical reaction.

$$Fe^{4+} + e^-_{cb} \rightarrow Fe^{3+} \quad (9)$$

$$Fe^{2+} + h^+_{vb} \rightarrow Fe^{3+} \quad (10)$$

Moreover, the large Fe particles in Fe-TNT4 could block the light reaching the underlying nanotubes, and thus lesser light was able to penetrate TNT to generate the photocurrent.

CONCLUSION

This work demonstrates a feasible way of depositing Fe on TiO_2 nanotube arrays using a simple electrochemical method. The morphological of ordered TiO_2 nanotubes was preserved when the deposition voltage was below 3 V. Different characterization techniques using FESEM, EDX, UV-Vis spectrum, and the photoelectrochemical test had proven that Fe was incorporated on TNT. An appropriate amount of deposited Fe (using 2-3 V in 0.1 M $FeCl_3$) is crucial to improve the photoelectrochemical performance of the prepared samples under visible light illumination.

ACKNOWLEDGEMENT

Financial support by Universiti Teknologi MARA under Geran Insentif Penyelidikan [600-IRMI 5/3/GIP (025/2018)] is gratefully acknowledged.

REFERENCES

1. Fujishima, A. & Honda, K. (1972) Electrochemical photolysis of water at a semiconductor electrode. *Nature*, **238(5358)**, 37–38.

2. Chen, S. H., Chan, S. H., Lin, Y. T. & Wu, M. C. (2019) Enhanced power conversion efficiency of perovskite solar cells based on mesoscopic Ag-doped TiO_2 electron transport layer. *Applied Surface Science*, **469**, 18–26.

3. Zubair, M., Kim, H., Razzaq, A., Grimes, C. A. & In, S. I. (2018) Solar spectrum photocatalytic conversion of CO_2 to CH_4 utilizing TiO_2 nanotube arrays embedded with graphene quantum dots. *Journal of CO_2 Utilization*, **26**, 70–79.

4. Li, G., Lv, L., Fan, H., Ma, J., Li, Y., Wan, Y. & Zhao, X. S. (2010) Effect of the agglomeration of TiO_2 nanoparticles on their photocatalytic performance in the aqueous phase. *Journal of Colloid and Interface Science*, **348(2)** , 342–347.

5. Nishanthi, S. T., Subramanian, E., Sundarakannan, B. & Padiyan, D. P. (2015) An insight into the influence of morphology on the photoelectrochemical activity of TiO_2 nanotube arrays. *Solar Energy Materials and Solar Cells*, **132**, 204–209.

6. Sekino, T. (2010) Synthesis and applications of titanium oxide nanotubes. In *Inorganic and Metallic Nanotubular Materials*, 17–32. Springer, Berlin, Heidelberg.

7. Gupta, S. M. & Tripathi, M. (2011) A review of TiO_2 nanoparticles. *Chinese Science Bulletin*, **56(16)**, 1639.

8. Mi, Q., Zhanaidarova, A., Brunschwig, B. S., Gray, H. B. & Lewis, N. S. (2012) A quantitative assessment of the competition between water and anion oxidation at WO_3 photoanodes in acidic aqueous electrolytes. *Energy & Environmental Science*, **5(2)**, 5694–5700.

9. Ayal, A. K. (2018) Enhanced photocurrent of titania nanotube photoelectrode decorated with CdS nanoparticles. *Baghdad Science Journal*, **15(1)**, 57–62.

10. Brahimi, R., Bessekhouad, Y., Bouguelia, A. & Trari, M. (2008) Improvement of eosin visible light degradation using PbS-sensititized TiO_2. *Journal of Photochemistry and Photobiology A: Chemistry*, **194(2-3)**, 173–180.

11. Chen, C., Ye, M., Lv, M., Gong, C., Guo, W. & Lin, C. (2014) Ultralong rutile TiO2 nanorod arrays with large surface area for CdS/CdSe quantum dot-sensitized solar cells. *Electrochimica Acta*, **121**, 175–182.

12. Paramasivam, I., Nah, Y. C., Das, C., Shrestha, N. & Schmuki, P. (2010) WO_3/TiO2 nanotubes with strongly enhanced photocatalytic activity.

Chemistry-A European Journal, **16(30**), 8993.

13. Chen, X. & Burda, C. (2008) The electronic origin of the visible-light absorption properties of C-, N-and S-doped TiO_2 nanomaterials. *Journal of the American Chemical Society*, **130**(**15**), 5018–5019.

14. Dong, Z., Ding, D., Li, T. & Ning, C. (2018) Ni-doped TiO_2 nanotubes photoanode for enhanced photoelectrochemical water splitting. *Applied Surface Science*, **443**, 321–328.

15. Kumaravel, V., Mathew, S., Bartlett, J. & Pillai, S. C. (2019) Photocatalytic hydrogen production using metal doped TiO_2: A review of recent advances. *Applied Catalysis B: Environmental*, **244**, 1021–1064.

16. Zhang, D., Chen, J., Xiang, Q., Li, Y., Liu, M. & Liao, Y. (2019) Transition-Metal-Ion (Fe, Co, Cr, Mn, Etc.) Doping of TiO_2 Nanotubes: A General Approach. *Inorganic chemistry*, **58(19**), 12511–12515.

17. Yu, J., Xiang, Q. & Zhou, M. (2009) Preparation, characterization and visible-light-driven photocatalytic activity of Fe-doped titania nanorods and first-principles study for electronic structures. *Applied Catalysis B: Environmental*, **90(3-4)**, 595–602.

18. Wantala, K., Tipayarom, D., Laokiat, L. & Grisdanurak, N. (2009) Sonophotocatalytic activity of methyl orange over Fe(III)/TiO_2. *Reaction Kinetics and Catalysis Letters*, **97**(**2)**, 249-254.

19. Bashiri, R., Samsudin, M. F. R., Mohamed, N. M., Suhaimi, N. A., Ling, L. Y., Sufian, S. & Kait, C. F. (2020) Influence of growth time on photoelectrical characteristics and photocatalytic hydrogen production of decorated Fe_2O_3 on TiO_2 nanorod in photoelectrochemical cell. *Applied Surface Science*, **510**, 145482.

20. Tong, X., Shen, W., Zhang, X., Corriou, J. P. & Xi, H. (2020) Synthesis and density functional theory study of free-standing Fe-doped TiO_2 nanotube array film for H_2S gas sensing properties at low temperature. *Journal of Alloys and Compounds*, 155015.

21. Wang, Q., Jin, R., Zhang, M. & Gao, S. (2017) Solvothermal preparation of Fe-doped TiO_2 nanotube arrays for enhancement in visible light induced photoelectrochemical performance. *Journal of Alloys and Compounds*, **690**, 139–144.

22. Zafar, Z. & Kim, J. (2020) Optimization of hydrothermal synthesis of Fe–TiO_2 nanotube arrays for enhancement in visible light using an experimental design methodology. *Environmental Research*, **189**, 109908.

23. Majeed Khan, M. A., Siwach, R., Kumar, S. & Alhazaa, A. N. (2019) Role of Fe doping in tuning photocatalytic and photoelectrochemical properties of TiO_2 for photodegradation of methylene blue. *Optics & Laser Technology*, **118**, 170–178.

24. Vasile, E., Sima, M., Sima, A. & Logofatu, C. (2020) TiO_2/Fe_2O_3 photoanodes for solar water oxidation prepared via electrodeposition of amorphous precursors. *Materials Research Bulletin*, **121**, 110623.

25. Chin, L. Y., Zainal, Z., Khusaimi, Z. & Ismail, S. S. (2016) Electrochemical synthesis of ordered titania nanotubes in mixture of ethylene glycol and glycerol electrolyte. *Malaysian Journal of Analytical Sciences*, **20(2)**, 373–381.

26. Wei, X., Wang, H., Zhu, G., Chen, J. & Zhu, L. (2013) Iron-doped TiO_2 nanotubes with high photocatalytic activity under visible light synthesized by an ultrasonic-assisted sol-hydrothermal method. *Ceramics International*, **39(4)**, 4009-4016.

27. Mancuso, A., Sacco, O., Sannino, D., Pragliola, S. & Vaiano, V. (2020) Enhanced visible-light-driven photodegradation of Acid Orange 7 azo dye in aqueous solution using Fe-N co-doped TiO_2. *Arabian Journal of Chemistry*, **13(11)**, 8347–8360.

28. Guaglianoni, W. C., Ruwer, T. L., Caldeira, L. E. N., Wermuth, T. B., Venturini, J. & Bergmann, C. P. (2021) Single-step synthesis of Fe-TiO_2 nanotube arrays with improved light harvesting properties for application as photoactive electrodes. *Materials Science and Engineering: B*, **263**, 114896.

29. Sun, L., Li, J., Wang, C. L., Li, S. F., Chen, H. B. & Lin, C. J. (2009) An electrochemical strategy of doping Fe^{3+} into TiO_2 nanotube array films for enhancement in photocatalytic activity. *Solar Energy Materials and Solar Cells*, **93(10)**, 1875–1880.